

PearSAN: A Machine Learning Method for Inverse Design using Pearson Correlated Surrogate Annealing

Michael Bezick Blake A. Wilson Vaishnavi Iyer Yuheng Chen Vladimir M. Shalaev Sabre Kais Alexander V. Kildishev Alexandra Boltasseva* Brad Lackey*

Michael Bezick¹, Blake A. Wilson^{1,2}, Vaishnavi Iyer^{1,2}, Yuheng Chen^{1,2}, Vladimir M. Shalaev^{1,2}, Sabre Kais^{1,2}, Alexander V. Kildishev¹, Alexandra Boltasseva^{1,2*}, Brad Lackey^{3*}

¹ Elmore Family School of Electrical and Computer Engineering, Birck Nanotechnology Center, and Purdue Quantum Science and Engineering Institute, Purdue University, West Lafayette, IN, 47907, USA

² Quantum Science Center, Oak Ridge National Laboratory, Oak Ridge, TN 37830, USA ³ Microsoft Quantum, Redmond, WA, USA

*Corresponding authors: aeb@purdue.edu, brad.lackey@microsoft.com

PearSAN is a machine learning-assisted optimization algorithm applicable to inverse design problems with large design spaces, where traditional optimizers struggle. The algorithm leverages a generative model’s latent space for rapid sampling and employs a Pearson correlated surrogate model to predict the figure of merit of the true design metric. As a showcase example, PearSAN is applied to thermophotovoltaic (TPV) metasurface design by matching the working bands between a thermal radiator and a photovoltaic cell. PearSAN can work with any pretrained generative model with a discretized latent space, making it easy to integrate with VQ-VAEs and binary autoencoders. Its novel Pearson correlational loss can be used as both a latent regularization method, similar to batch and layer normalization, and as a surrogate training loss. We compare both to previous energy matching losses, which are shown to enforce poor regularization and performance, even with upgraded affine parameters. PearSAN achieves a state-of-the-art maximum design efficiency of $\sim 97\%$ and is at least an order of magnitude faster than previous methods, with an improved maximum figure-of-merit gain.

1 Introduction

With the impressive capabilities of modern generative models, including Generative Adversarial Networks (GANs) [1, 2], diffusion models [3–5], and Large Language Models [6–8], there is growing interest in their application across various engineering domains. GANs and diffusion models have shown potential for generating device designs with specific properties by integrating surrogate models in place of large and complex simulations. Surrogate optimization algorithms can be applied to many engineering challenges, such as topology optimization for mechanical or architectural components, novel 3D circuit layouts, and predicting failure modes in intricate systems. These models make efficient use of synthetic training datasets, helping reduce simulation costs and shorten design cycles [9–13].

In photonics and optoelectronics, the optimization of new compact planar devices and systems built on optical metasurfaces is a nascent engineering problem [10,14–19]. Optical metasurfaces are subwavelength-thin nanostructured films that have fine-tuned control over phase, amplitude, and polarization across various wavelengths through a composition of optimized meta-atoms. Their unique properties have sparked tremendous interest in tailoring metasurfaces for emerging applications in sensing [20–22], quantum information [11, 23], and renewable energy [24]. Traditional methods of generating optimal meta-atoms for tailored metasurfaces requires computationally expensive gradient calculations in an exponentially large design space, making direct optimization impractical [25]. Alternative to these approaches is *latent optimization* [10, 15, 17], an ever-growing suite of machine learning-assisted optimization algorithms that sample designs for optimization problems from a feature-rich, lower-dimensional latent space using global search algorithms such as simulated annealing [26], stochastic gradient descent, Markov Chain Monte Carlo [10, 11] or quantum-inspired optimizers [27]. Often these latent optimization algorithms use a pretrained decoder and train a surrogate model to predict the figure-of-merit of a decoded design solely from its latent vector. Then, optimizing the input to the surrogate model generates latent vectors, which are decoded into designs with low loss and good figure-of-merit. The choice of surrogate model, surrogate loss, latent space regularization, and surrogate optimizer is crucial for latent optimization performance. For example, in the original bVAE-QUBO work [10], a pretrained binary variational autoencoder (bVAE) with Gumbel-Softmax reparameterization [28] created a categorical distribution over la-

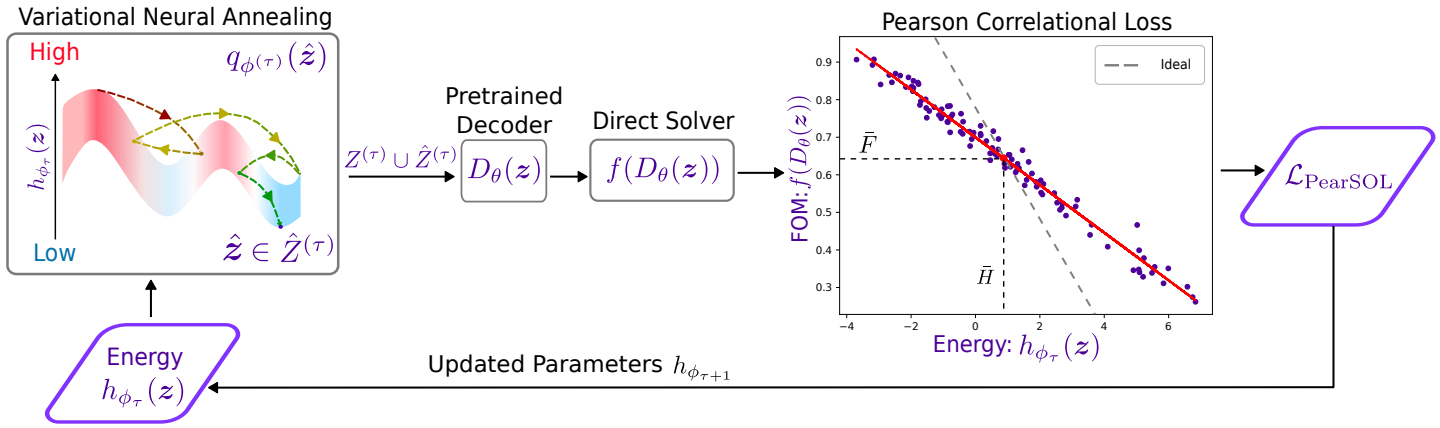


Figure 1: **PearSAN** starts with an initial dataset $Z^{(0)}$. The generated polynomial $h_{\phi(\tau)}(z)$ is then used in variational neural annealing to train the sampler $q_{\phi(\tau)}(z)$ by minimizing its free energy $F_{\phi(\tau)}(t)$. The resultant latent vectors \hat{z} are then stored in a database. The sampler is then evaluated through the pretrained decoder, which generates real samples $D_{\theta}(\hat{z})$. The samples' efficiency is computed through a direct solver, represented by the grey area between the ideal and resultant spectra. The efficiency $f(D_{\theta}(\hat{z}))$, along with its corresponding sample, are also stored in the database. The Pearson correlational loss is informed through the database, which constitutes an antitonic correlation between $h_{\phi(\tau)}(z)$ and $f(D_{\theta}(\hat{z}))$. The resultant Pearson value is used to update the parameters of the surrogate model in the next iteration $\phi^{(\tau+1)}$, and the process is repeated.

tent vectors, which generated meta-atom designs. Then, a surrogate QUBO model was trained on binary vectors to predict the design efficiency of the generated designs using an *energy matching* (EM) loss. Sampling the QUBO model using a hybrid quantum sampler generated latent vectors which were decoded into optimal designs through the pretrained decoder. Resampling and retraining refined the surrogate QUBO model, leading to better design efficiencies. As we address in this work, the FOM generated throughout resampling was very noisy and weakly correlated through categorical regularization and EM loss. Additionally, the hybrid quantum/classical sampler and simulated annealing used in bVAE-QUBO can be replaced by faster recurrent neural networks through variational neural annealing, speeding up surrogate sampling.

In this work, we address some limitations of previous latent optimization algorithms by introducing Pearson Correlated Surrogate Annealing (PearSAN) in Section 2.5. We demonstrate PearSAN on the thermophotovoltaic (TPV) cell design problem by optimizing the working band of a thermal emitter to achieve high overlap efficiency with the absorption band of an ideal photovoltaic cell. The only degree of freedom is the material topology of the thermal emitter composed of TiN distributed on a Si_3N_4 spacer. By formalizing the latent optimization problem in Section 2.1 with Bayesian techniques, we introduce an antitonic training objective, requiring antitonicity between our optimizer and a surrogate model, and thus isotonicity with FOM, which are all fully satisfied with PearSAN. Isotonic or antitonic regressions sit between a simple linear regression (enforcing linearity) and fully non-parametric methods (which make no assumptions about the relationship's shape). These approaches are particularly useful when the intrinsic physics suggests a monotonic relationship, but the exact form is unknown. The fundamental assumption is that the relationship between the predictor and the response is monotonic, i.e., consistently increasing (isotonic) or decreasing (antitonic).

First, we marginalize the latent distribution in the training objective over a pretrained deterministic decoder in Section 2.2, simplifying the isotonicity requirements. Then, we introduce variational neural annealing [29] in Section 2.3 with a pseudo-boolean polynomial surrogate model to antitonicly sample the surrogate model, which has demonstrated significant performance benefits over simulated annealing and other discrete global optimizers. Finally, we introduce the Pearson Correlated Surrogate Optimization Loss (PearSOL) in Section 2.4 to enforce antitonicity between the surrogate model and the FOM while improving on EM in both decoder regularization and surrogate model training. While PearSAN and other latent optimization algorithms work with an unregularized, pretrained decoder, as evidence

by bVAE-QUBO, we explore the use of EM and PearSOL for regularization¹. PearSOL only enforces that a larger design FOM implies a larger surrogate model value of the corresponding latent vector, and hence the more probable to be generated, i.e., a design’s probability is isotonic with its FOM, whereas EM enforces that the surrogate model value of a design must be close to the FOM. We compare both losses in Section 3 by optimizing meta-atoms for thermal emitters in a thermophotovoltaic cell, which convert residual heat into usable electricity. We show that EM leads to weaker regularization through KID, FID and Inception score, and worse optimization performance. PearSOL is less restrictive, leading to better regularization and sampling quality.

2 Methods

2.1 Isotonic Latent Optimization

Consider a data space \mathcal{X} sampled i.i.d. $X = \{\mathbf{x}^{(i)}\}_{i=1}^N$ where each point $\mathbf{x}^{(i)}$ has a figure-of-merit (FOM) value $f(\mathbf{x}^{(i)})$. Our goal is to train a generative model p_θ with variational parameters θ to sample new data $\hat{\mathbf{x}} \sim p_\theta(\hat{\mathbf{x}})$ that optimizes the expected FOM $f(\cdot)$, i.e.,

$$\arg \max_{\theta} \mathbb{E}_{\hat{\mathbf{x}} \sim p_\theta(\hat{\mathbf{x}})} [f(\hat{\mathbf{x}})]. \quad (1)$$

Since the advent of variational autoencoders [30, 31], many generative models rely on extracting data features into a low-dimensional *latent* space \mathcal{Z} with latent variables $\mathbf{z} \in \mathcal{Z}$ [5]. Then, the new data is sampled directly from the latent space \mathcal{Z} using a conditional decoder $\hat{\mathbf{x}} \sim p_\theta(\hat{\mathbf{x}}|\mathbf{z})$. To leverage latent sampling for optimization, we express $p_\theta(\hat{\mathbf{x}}) = \sum_{\mathbf{z}} p_\theta(\hat{\mathbf{x}}|\mathbf{z})q_\phi(\mathbf{z})$ with a latent sampler $q_\phi(\mathbf{z})$ and latent variational parameters ϕ . Then, we rewrite Eq. 1 as a latent optimization problem

$$\arg \max_{\theta, \phi} \mathbb{E}_{\mathbf{z} \sim q_\phi(\mathbf{z})} [\mathbb{E}_{\hat{\mathbf{x}} \sim p_\theta(\hat{\mathbf{x}}|\mathbf{z})} [f(\hat{\mathbf{x}})]]. \quad (2)$$

This splits our model p_θ into a latent optimization sampler q_ϕ and a decoder $p_\theta(\hat{\mathbf{x}}|\mathbf{z})$. Rather than train the decoder being aware of the latent sampler’s optimization distribution q_ϕ [17], which can lead to sampling an unnormalized distribution at each gradient step [32] and meticulous fine-tuning problems [8], we train the latent sampler to produce optimal latent vectors under a pretrained “optimization-agnostic” decoder $p_\theta(\hat{\mathbf{x}}|\mathbf{z})$.²

The optimal latent sampler q_ϕ would solve Eq. 1 by producing the latent vector for a decoded design with the maximal FOM with probability 1, however this is generally infeasible to accomplish in practice because of the typically exponentially large latent space [33]. Instead, we only make the weak assumption that our model p_θ produces samples whose probability is (strictly) isotonic³ with the FOM values over the design space. We say that p_θ is (strictly) isotonic with f over \mathcal{X} , i.e., $f(\hat{\mathbf{x}}) \prec_{\mathcal{X}}^+ p_\theta(\hat{\mathbf{x}})$, to mean that for each pair of points $(\hat{\mathbf{x}}^{(i)}, \hat{\mathbf{x}}^{(j)}) \in \mathcal{X} \times \mathcal{X}$ we have⁴

$$f(\hat{\mathbf{x}}^{(i)}) < f(\hat{\mathbf{x}}^{(j)}) \implies p_\theta(\hat{\mathbf{x}}^{(i)}) < p_\theta(\hat{\mathbf{x}}^{(j)}). \quad (3)$$

By Eq. 3, the model will assign larger probability to samples with larger FOM values. With the fixed decoder $p_\theta(\hat{\mathbf{x}}|\mathbf{z})$, we expand the marginal of p_θ in Eq. 3 to obtain $f(\hat{\mathbf{x}}) \prec_{\mathcal{X}}^+ \sum_{\mathbf{z}} [p_\theta(\hat{\mathbf{x}}|\mathbf{z})q_\phi(\mathbf{z})]$. As we will show, to isotonicly couple the latent sampler q_ϕ to $f(\hat{\mathbf{x}})$, we pick a sampler q_ϕ that produces samples with probability isotonic to a surrogate function $h_\phi(\mathbf{z})$, i.e., $h_\phi(\mathbf{z}) \prec_{\mathcal{Z}}^+ q_\phi(\mathbf{z})$ over the latent space \mathcal{Z} . Then, we train the latent sampler’s surrogate function h_ϕ to be isotonic with f with respect to

¹This still means that the pretrained decoder is “optimization-agnostic” because the prior on the latent vectors for the decoder are not optimizing the objective throughout training.

²In principle, one could apply PearSAN or other latent optimization techniques to any pretrained decoder if its latent space is discrete. Future work will focus on the continuous case.

³That is, the larger the FOM the more probable the design.

⁴For minimization problems, we use $f(\hat{\mathbf{x}}) \prec_{\mathcal{X}}^- p_\theta(\hat{\mathbf{x}})$ to denote antitonic relationships $f(\hat{\mathbf{x}}^{(i)}) < f(\hat{\mathbf{x}}^{(j)}) \implies p_\theta(\hat{\mathbf{x}}^{(i)}) > p_\theta(\hat{\mathbf{x}}^{(j)})$.

Algorithm 1 PearSAN with Pretrained Decoder

-
- 1: **Require:** Initial dataset $Z^{(0)} = \{\mathbf{z}^{(i)}\}$
 - 2: **Require:** Pretrained decoder $\mathcal{D} : \mathcal{Z} \rightarrow \mathcal{X}$
 - 3: **Require:** Figure-of-merit $f : \mathcal{X} \rightarrow \mathbb{R}$
 - 4: **Require:** Iterations τ_{\max} .
 - 5: **for** $\tau \in [0, \dots, \tau_{\max} - 1]$ **do**
 - 6: $F^{(\tau)} \leftarrow \{f(\mathcal{D}(\mathbf{z}^{(i)})) : \forall \mathbf{z}^{(i)} \in Z^{(\tau)}\}$
 - 7: $H^{(\tau)} \leftarrow \{h_{\phi^{(\tau)}}(\mathbf{z}^{(i)}) : \forall \mathbf{z}^{(i)} \in Z^{(\tau)}\}$
 - 8: $h_{\phi^{(\tau)}} \leftarrow \mathcal{L}_{\text{PearSOL}}(F^{(\tau)}, H^{(\tau)})$ (Train surrogate model)
 - 9: $\hat{Z}^{(\tau)} \leftarrow \min(h_{\phi^{(\tau)}}(T))$ (Train and sample throughout VCA)
 - 10: $Z^{(\tau+1)} \leftarrow Z^{(\tau)} \cup \hat{Z}^{(\tau)}$ (Update Dataset)
 - 11: **end for**
 - 12: **Output:** Optimized design $X^{(\tau_{\max})} = \{\mathcal{D}_{\theta}(\mathbf{z}^{(i)}) : \mathbf{z}^{(i)} \in Z^{(\tau_{\max})}\}$.
-

a marginal over the latent space to achieve

$$\begin{aligned}
 f(\hat{\mathbf{x}}) &\prec_{\mathcal{X}}^+ \sum_{\mathbf{z}} [p_{\theta}(\hat{\mathbf{x}}|\mathbf{z})h_{\phi}(\mathbf{z})] \\
 &\prec_{\mathcal{X}}^+ \sum_{\mathbf{z}} [p_{\theta}(\hat{\mathbf{x}}|\mathbf{z})q_{\phi}(\mathbf{z})].
 \end{aligned} \tag{4}$$

Training q_{ϕ} and h_{ϕ} under these isotonic conditions is difficult because the decoder is often optimization-agnostic, meaning it isn't a priori trained to favor designs with large FOM, making it easy to break the isotone requirement in the worst case. However, if the pretrained decoder is deterministic, as is often the case, then we can marginalize Eq. 4 to be more tractable.

2.2 Pretrained Deterministic Decoder

In practice, decoders $p_{\theta}(\hat{\mathbf{x}}|\mathbf{z})$ are often deterministic, meaning a fixed model \mathcal{D}_{θ} produces a single design from each latent vector, i.e., $\mathcal{D}_{\theta}(\mathbf{z}) \equiv \hat{\mathbf{x}}$. The deterministic decoder distribution can be rewritten as $p_{\theta}(\hat{\mathbf{x}}|\mathbf{z}) = P(\hat{\mathbf{x}} = \mathcal{D}_{\theta}(\mathbf{z}))$ which is 1 for the decoded design and 0 for all other designs. Using this fact, we marginalize over \mathbf{z} to reduce Eq. 4 to

$$\begin{aligned}
 f(\hat{\mathbf{x}}) &\prec_{\mathcal{X}}^+ h_{\phi}(\mathcal{D}^{-1}(\hat{\mathbf{x}})) \prec_{\mathcal{X}}^+ q_{\phi}(\mathcal{D}^{-1}(\hat{\mathbf{x}})) \\
 &\iff f(\mathcal{D}(\hat{\mathbf{z}})) \prec_{\mathcal{Z}}^+ h_{\phi}(\hat{\mathbf{z}}) \prec_{\mathcal{Z}}^+ q_{\phi}(\hat{\mathbf{z}}),
 \end{aligned} \tag{5}$$

where $\mathcal{D}_{\theta}^{-1}$ is the inverse of \mathcal{D}_{θ} . The deterministic decoder has the benefit of coupling the figure-of-merit directly to the latent sampler through the surrogate model.

Our focus is now on realizing the isotonic conditions in Eq. 5. by 1) choosing a distribution q_{ϕ} that is isotonic with a trainable surrogate model h_{ϕ} and 2) enforcing that the surrogate model h_{ϕ} is isotonic with the FOM values, i.e., $f(\hat{\mathbf{x}}) \prec_{\mathcal{X}}^+ h_{\phi}(\mathbf{z})$, both of which are satisfied with PearSAN.

2.3 Variational Neural Annealing

The most popular samplers q_{ϕ} which aim to produce samples isotonic with a surrogate function are Markov Chain Monte Carlo [11], simulated annealing [26], quantum samplers [34], and more recently variational neural annealing [29]. Inspired by statistical mechanics, these samplers are *antitonic* to an energy model $h_{\phi}(\mathbf{z}) \prec_{\mathcal{Z}}^- q_{\phi}(\mathbf{z})$ where $\mathcal{Z} = \{0, 1\}^n$ and h_{ϕ} is given by a pseudo-boolean polynomial,

$$\begin{aligned}
 h_{\phi}(\mathbf{z}) &= \sum_{s \subseteq n} \phi_s \prod_{i \in s} z_i \\
 &= \sum_i \phi_i z_i + \sum_{i < j} \phi_{i,j} z_i z_j + \sum_{i < j < k} \phi_{i,j,k} z_i z_j z_k \dots
 \end{aligned} \tag{6}$$

typically representing the potential interactions between spin sites [35], superconducting rings [34], etc. To construct $q_\phi(\mathbf{z})$, we implement variational classical annealing (VCA), a variant of variational neural annealing. VCA uses recurrent neural networks (RNNs) to sample $h_\phi(\mathbf{z})$ with better practical convergence compared to Markov Chain Monte Carlo and simulated annealing [29], as we corroborate in Appendix 9. RNNs are widely used for generating sequential data, such as language modeling [36], anomaly detection [37], and biometric authentication [38] through autoregression. The RNN's structure is modeled after the chain rule of probability, where the output joint probability distribution $q_\phi(\mathbf{z})$ can be expressed as

$$q_\phi(\mathbf{z}) = q_\phi(z_1)q_\phi(z_2|z_1) \dots q_\phi(z_N|z_{N-1}, \dots, z_1). \quad (7)$$

Each bit z_i in the latent vector \mathbf{z} is generated by a conditional probability statement $q_\phi(z_i|z_1, \dots, z_{i-1})$ following a Bernoulli distribution. VCA works through *minimizing* the sampler's variational free energy

$$G_\phi(t) = \mathbb{E}_{\mathbf{z} \sim q_\phi(\mathbf{z})}[h_\phi(\mathbf{z})] - T(t)S(q_\phi), \quad (8)$$

where $T(t)$ is a temperature parameter that is decreased through the annealing process from a large $T(0) = T_0$ to 0, and $S(q_\phi) = -\sum_{\mathbf{z}} q_\phi(\mathbf{z}) \log(q_\phi(\mathbf{z}))$ is the entropy. We approximate the variational free energy at temperature T as

$$G_\phi(T) \approx \frac{1}{N_s} \sum_{i=1}^{N_s} h_\phi(\mathbf{z}^{(i)}) + T \log(q_\phi(\mathbf{z}^{(i)})), \quad (9)$$

by taking N_s discrete samples drawn from the RNN, i.e., $\mathbf{z}^{(i)} \sim q_\phi$. The $T \log(q_\phi(\mathbf{z}^{(i)}))$ term has the effect of enforcing more randomness in the state evolution during the beginning of training with a high T , allowing the model to escape local minima and increasing the entropy throughout the annealing process. As T decreases, analogous to simulated annealing, the model is less likely to exhibit large, random changes of state, favoring to minimize the surrogate function, implying that $h_\phi(\mathbf{z}) \prec_{\mathbf{z}}^- q_\phi(\mathbf{z})$. To allow for the antitonicity of VCA, we replace the isotonic relations in Eq. 5 with antitonic relations while still maintaining the overall objective, i.e.,

$$f(\mathcal{D}(\hat{\mathbf{z}})) \prec_{\mathbf{z}}^- h_\phi(\mathbf{z}) \quad (10)$$

$$h_\phi(\mathbf{z}) \prec_{\mathbf{z}}^- q_\phi(\mathbf{z}) \quad (11)$$

$$\implies f(\mathcal{D}_\theta(\hat{\mathbf{z}})) \prec_{\mathbf{z}}^+ q_\phi(\mathbf{z}), \quad (12)$$

where Eq. 11 is satisfied by using VCA. To enforce Eq. 10, we introduce PearSOL.

2.4 Pearson Surrogate Optimization Loss (PearSOL)

Training an antitonic surrogate model typically involves modifying the *energy matching* (EM) loss, which uses a pairwise L-norm loss function [10], e.g.,

$$\mathcal{L}_{\text{EM}}(F, H) = \sum_i \|F_i - (-H_i)\|_2^2, \quad (13)$$

where $F = \{f(\mathcal{D}_\theta(\mathbf{z}^{(i)}))\}_{i=1}^n$ represents the set of decoded FOMs and $H = \{h_\phi(\mathbf{z}^{(i)})\}_{i=1}^n$ represents the latent vector energies. EM minimizes the difference between $-H^{(i)}$ and $F^{(i)}$, thus achieving antitonicity, but L-norm loss can be overly sensitive in less-explored regions and unnecessarily penalizes small differences. To overcome these issues and enforce antitonicity, we propose using Pearson correlation [39, 40]:

$$\mathcal{L}_{\text{Pearson}}(F, H) = \frac{\sum_i (F_i - \bar{F})(H_i - \bar{H})}{\hat{S}_F \hat{S}_H} \quad (14)$$

where \bar{H} and \hat{S}_H are the mean and standard deviation of H , and \bar{F} and \hat{S}_F are defined similarly for F . By the Cauchy-Schwarz inequality, $\mathcal{L}_{\text{Pearson}}(F, H) \in [-1, 1]$, with +1 or -1 indicating perfect isotonic or

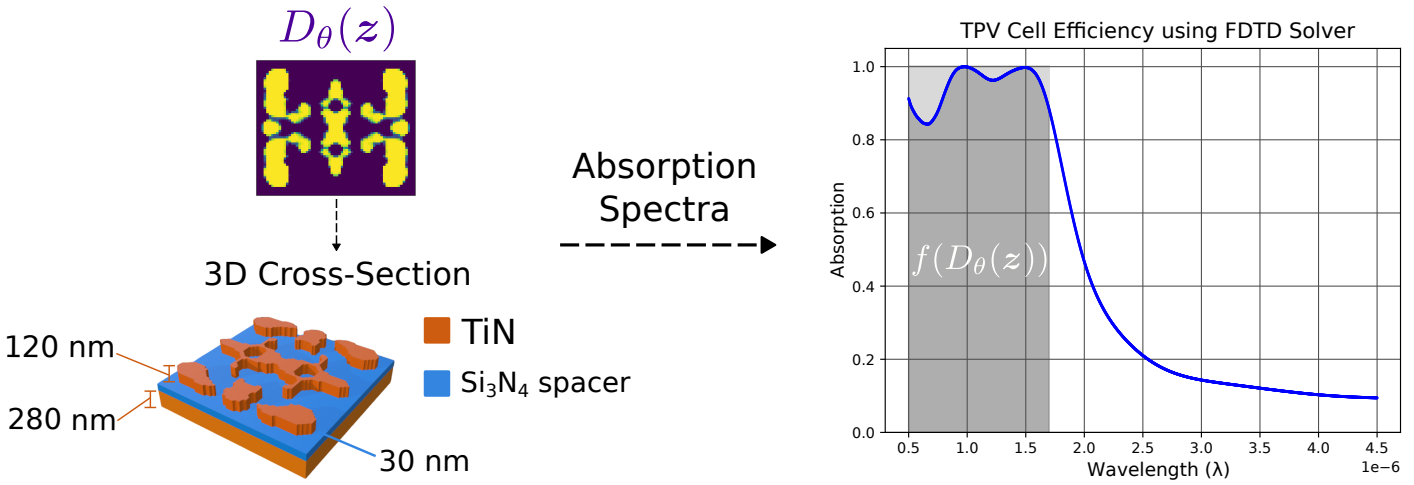


Figure 2: **Thermophotovoltaic Cells:** The TPV cells considered in our showcase problem correspond to the samples $D_\theta(\mathbf{z})$ generated by the pretrained decoder, and consist of a thermal emitter and photovoltaic cell. The thermal emitter converts thermal energy into photons, and the photovoltaic cell generates electricity from these photons within a specific wavelength. Each thermal emitter consists of 3 layers: a 120nm titanium nitride plasmonic antenna, a 30nm silicon nitride spacer, and a 280nm wide titanium nitride back reflector, as shown in the 3D cross-section. The topology of each thermal emitter determines its radiation spectrum, which ideally falls solely within the working band of the photovoltaic. The generated thermal emitter efficiencies are assessed either through a regression model-based VGGNet during training and FDTD simulation after sampling. The grey area on the graph indicates the working band, and the darker area underneath the spectra curve shows the efficiency $f(D_\theta(\mathbf{z}))$ of the cell.

antitonic correlations, respectively (See Appendix 6). Our goal is to achieve a Pearson correlation of -1 , achieving antitonicity $f(\mathcal{D}(\mathbf{z})) \prec_{\mathcal{Z}} h_\phi(\mathbf{z})$. In practice, gradient convergence requires hyperparameter tuning and a supplementary inverse logistic curve (see Appendix 7).

To improve the antitonicity and the lower-energy distribution of points, we impose an additional regularization loss in the form of an average energy loss $\mathcal{L}_{\text{Avg}}(H) = \overline{H}$ which simply minimizes the average energy. However, to ensure that the surrogate model's parameters remain near 1 and maintain the norm of h_ϕ , we add a regularization term $\mathcal{L}_{\text{Norm}}$, lest \mathcal{L}_{Avg} is satisfied through exploding negative energy function parameters. Our full PearSOL function reads,

$$\mathcal{L}_{\text{PearSOL}} = \lambda_a \mathcal{L}_{\text{Pearson}} + \lambda_b \mathcal{L}_{\text{Avg}} + \lambda_c \mathcal{L}_{\text{Norm}}, \quad (15)$$

with hyperparameters $\lambda_a, \lambda_b, \lambda_c$ and each loss implicitly using H and F where appropriate.

2.5 PearSAN Overview

PearSAN is especially effective when the initial dataset $X^{(0)}$ is updated with new designs generated by the decoder, allowing the surrogate model to retrain on the FOM from the new designs. We denote the current iteration with τ and the total iterations with τ_{max} . As outlined in Alg. 1, we begin by sampling an initial set of latent vectors $Z^{(0)} = \{\mathbf{z}^{(i)}\}$ either via an encoder $\mathbf{z}^{(i)} \sim \mathcal{E}(\mathbf{x}^{(i)}) : \mathbf{x}^{(i)} \in X^{(0)}$ or some prior $\mathbf{z}^{(i)} \sim q(\mathbf{z})$. Each iteration begins by training a polynomial surrogate model $h_{\phi(\tau)}$ (Eq. 6) to optimize the PearSOL over $Z^{(\tau)}$, $\mathcal{L}_{\text{PearSOL}}(F^{(\tau)}, H^{(\tau)})$ where

$$H^{(\tau)} = \{h_{\phi(\tau)}(\mathbf{z}^{(i)}) : \mathbf{z}^{(i)} \in Z^{(\tau)}\} \quad (16)$$

$$F^{(\tau)} = \{f(\mathcal{D}_\theta(\mathbf{z}^{(i)})) : \mathbf{z}^{(i)} \in Z^{(\tau)}\}, \quad (17)$$

and \mathcal{D}_θ is a pretrained, deterministic decoder $\mathcal{D}_\theta(\mathbf{z})$ with a discrete latent space. Then, we train a RNN $q_{\phi(\tau)}$ to antitonicly sample the surrogate model h_{ϕ_τ} using VCA by minimizing Eq. 9. As evidenced by the success of dropout, score matching and diffusion models, adding noise throughout training can promote exploration and larger accuracy in lower-probability regions of the latent space. For VCA, the high

	KID ↓	FID ↓	Inception Score ↑
EM	0.067	54.67	1.99
PearSOL	0.063	52.57	2.04

Table 1: Comparison of two bAEs, one regularized with EM and one with PearSOL, across KID, FID, and Inception Score metrics. Scores are computed using 20,000 unique vectors generated from a complete VCA traversal.

temperature $T = T_0$ noisy sampling at the beginning of training operates to both aid the annealing process and increase the breadth of sampled latent vectors. Therefore, we accumulate latent vectors $\hat{Z}^{(\tau)}$ throughout the noisy VCA steps to allow the surrogate model to learn both breadth and depth of the latent space’s relation to the FOM. Practically, we set an epoch cutoff N_{thresh} , before collecting latent vectors for training to exclude vectors generated at excessively high temperatures which are less responsive to $h_{\phi(\tau)}$. We accumulate the new latent vectors $\hat{Z}^{(\tau)} = \{\hat{z}^{(i)}\} : \hat{z} \sim q_{\phi(\tau)}(\hat{z})$ and construct a new dataset $Z^{(\tau+1)} = Z^{(\tau)} \cup \hat{Z}^{(\tau)}$. We repeat this procedure a total of τ_{max} times.

3 Experimental Setup and Results

To empirically test PearSAN, we compare the reported designs and runtimes against existing optimization methods for the TPV design problem. Additionally, we perform an ablation study to understand the importance of PearSOL for PearSAN. We demonstrate that for both regularizing a decoder during pretraining and training a surrogate model, PearSOL is favorable to EM. For all loss function comparisons, we use the same hyperparameters, TPV unit cell dataset, architectures for the binary autoencoder (bAE) and RNN, and optimizer temperature schedule. In Appendix 5.2, we attempt to upgrade EM with positive affine parameters over the surrogate model to help EM yield similar results to PearSOL. However, we find that the affine parameters make training worse, likely due to fine tuning difficulties. These of training and superior quality in both decoder scores and optimization quality reinforces our choice of PearSOL for PearSAN.

3.1 TPV Optimization Setup

We consider the problem of unit-cell topology optimization of thermal emitters for thermophotovoltaics (TPVs), demonstrated in Fig. 2. TPVs generate electricity from thermal radiation, but they are and are currently able to achieve efficiencies of around 40% [10, 41]. As conventional power generation techniques waste a large amount of heat to the environment, TPVs provide a convenient method of capturing this residual heat and converting it to useable electricity [24]. TPVs contain a thermal emitter that converts heat into photons, with the primary goal of emitting the highest percentage of photons within the working band wavelength of the photovoltaic (PV) cell [42]. We consider gallium antimonide PV cells, with a working band from $\lambda_{\text{min}} = 0.5\mu\text{m}$ to $\lambda_{\text{max}} = 1.7\mu\text{m}$. We focus on the optimization of a thermal emitter topology with a titanium nitride plasmonic antenna, 30nm silicon nitride spacer, and titanium nitride back reflector. The configuration of air and raised antenna determines the spectral emissivity. Each TPV unit cell design, denoted as $\mathbf{x} \in \{0, 1\}^{64 \times 64}$, is represented by a 64×64 binary grid where 1 corresponds to a raised TiN antenna, and 0 corresponds to an air gap. A binary autoencoder (bAE) is pretrained, as described in Appendix 8, using a dataset of 12,000 topology-optimized designs constructed through costly adjoint optimization methods [17]. The initial latent vector dataset $Z^{(0)}$ is generated by sampling from the bAE encoder, i.e., $\mathbf{z}^{(i)} \sim \text{Bernoulli}(\mathcal{E}(\mathbf{x}^{(i)}))$ (see Appendix 8). For evaluating the figure of merit (FOM) $f(\mathbf{x})$, we use a fast, pretrained VGGNet regression model, and note that the output FOM is unnormalized, hence plots are not scaled to 1.

3.2 Impact of Regularization

We assess the effectiveness of PearSOL and EM in regularizing the latent space of the bAE. As outlined in Appendix 8, regularization, while not strictly necessary for PearSAN’s operation, helps improve sample quality by avoiding overfitting during training. To evaluate regularization performance, we employ standard GAN evaluation metrics such as KID [43], FID [44], and Inception Score [45].

KID and FID measure the discrepancy between the features of generated and real datasets using a pre-trained neural network, with KID being less sensitive to sample size, making it preferable given our relatively small dataset of 12,000 designs. Inception Score evaluates the quality of generated samples by assessing their distinctiveness and diversity using a classification model [46]. As shown in Table 1, PearSOL outperforms EM in all metrics, indicating its ability to generalize across unseen regions of the latent space better than EM.

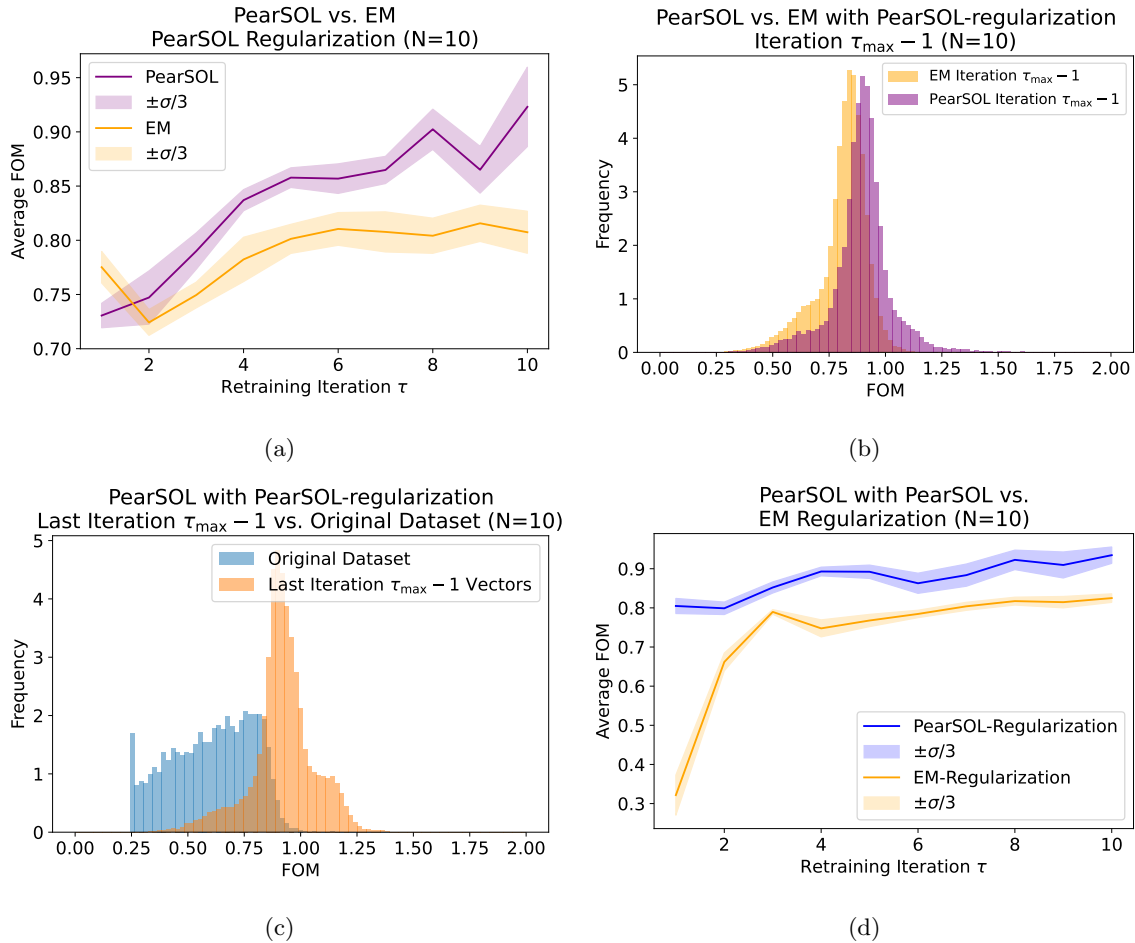


Figure 3: Retraining performance for PearSOL and EM: (a) Average sampled FOM over 10 retraining iterations, (b) FOM histogram of all decoded vectors from the last iteration, (c) Comparison of FOM between vectors generated by PearSOL and the original dataset (unnormalized VGGnet FOM), (d) Regularization performance of PearSOL versus EM.

3.3 Retraining Procedure

We consider $\tau_{\max} = 10$ iterations of PearSAN and a sampling epoch threshold at $N_{thresh} = 20$ for VCA, as indicated by convergence plots in Figure 9. For each retraining iteration, we average the FOM of all accumulated vectors across 10 experiments, excluding the first iteration where the surrogate model is under-trained due to random initialization. Figure 3 (a) shows that PearSOL consistently outperforms EM⁵ for all retraining iterations, achieving an average of 92.31% VGG-predicted efficiency on the final

⁵We use PearSOL as a regularization function in a bAE for both methods due to both models performing better as elaborated upon further in Figure 5.

Method	Efficiency (%) \uparrow	Time per 100 designs (hours) \downarrow	Designs per minute \uparrow
Direct Topology Optimization [15]	92.00	164	0.0102
AAE + VGGNet [15]	95.50	0.0333	50.1
AAE + TO* [15]	97.90	54	0.031
AAE + DE [17]	95.90	23.33	0.0714
AAE + rDE [17]	96.40	23.33	0.0714
bVAE-QUBO [10]	96.70	0.30	5.556
PearSAN (PearSOL)	97.02	0.0033	501.10

Table 2: Comparison of PearSAN (PearSOL) with previous optimization methods in terms of design efficiency and sampling time. The proposed method shows a significant speed improvement while achieving the highest efficiency outside of AAE+TO. However, AAE+TO and Direct Topology Optimization used FDTD simulations to perform adjoint optimization for fine-tuning and not the VGG model used in most other methods.

retraining iteration $\tau_{\max} - 1$, versus energy matching with an average of 80.74%. In the experiment of Figure 3 (b), we conduct a Welch two sample t-test comparing the mean FOM values from the final iteration τ_{\max} of PearSOL (85.81%) versus EM (79.08%), finding that PearSOL significantly outperformed EM ($t(607375) = 203.51, p < 2.2 \times 10^{-16}$). Furthermore, we consider both losses on two bAEs, one regularized with PearSOL and one with EM loss with affine parameters in Figure 5. We find that both models perform better utilizing the PearSOL-trained bAE, further corroborating our expectations from Table 1. In Figure 5 (a), we find that EM loss during retraining with EM regularization performed especially poorly, worsening in average FOM output during the retraining process. Additionally, EM with PearSOL regularization demonstrated significant variance and produced a bimodal distribution in Figure 5 (b) (for further discussion, see Appendix 5.2). In Figure 3 (c), we show how our technique significantly improves upon the quality of our dataset (mean 92.32% versus 60.54%).

3.4 Comparison with Previous Methods

We compare PearSAN’s efficiency against previous methods such as direct topology optimization [15], AAE+TO, AAE+VGGNet [15], AAE+DE, AAE+rDE [17] and bVAE-QUBO [10]. To generate the optimal design for PearSAN, we took the 100 best designs from the best run of PearSAN with PearSOL and simulated them using the same finite different time domain methods as the other techniques. While previous methods evaluated 100 designs over several hours, our PearSAN model evaluated 100 designs in just 0.0033 hours, showing a significant improvement in efficiency and sampling speed. PearSOL achieved the highest efficiency of 97.02%, outperforming all prior approaches which were limited by the VGGnet for predicting the FOM⁶. It should be noted that AAE+TO had direct access to FDTD calculations throughout training [17], whereas PearSAN had access to only the VGGnet. Comparing PearSAN to AAE+VGGnet, which is equivalent to AAE+TO except with the VGGnet, reveals that PearSAN may outperform AAE+TO either given a better FOM approximation network or direct access to FDTD simulations.

PearSAN’s efficiency and speed are orders of magnitude better than previous approaches, as shown in Table 2. This is likely due to the algorithmic performance improvements rather than hardware alone, though further study is required for a fair comparison of hardware advancements.

4 Conclusion and Outlook

In this work, we introduced **PearSAN**, a novel machine learning-assisted optimization algorithm for inverse design problems with large parameter spaces, as exemplified by our showcase example of optimizing the metasurface unit-cell design for thermophotovoltaics (TPVs). By pairing **Pearson Surrogate Optimization Loss (PearSOL)** regularization with **Variational Classical Annealing (VCA)** sampling, PearSAN leverages a discretized latent space (e.g., from VQ-VAEs or binary autoencoders) to gen-

⁶We include a precision of 10^{-2} for comparison purposes even though fabrication will introduce errors of $\pm 5\%$

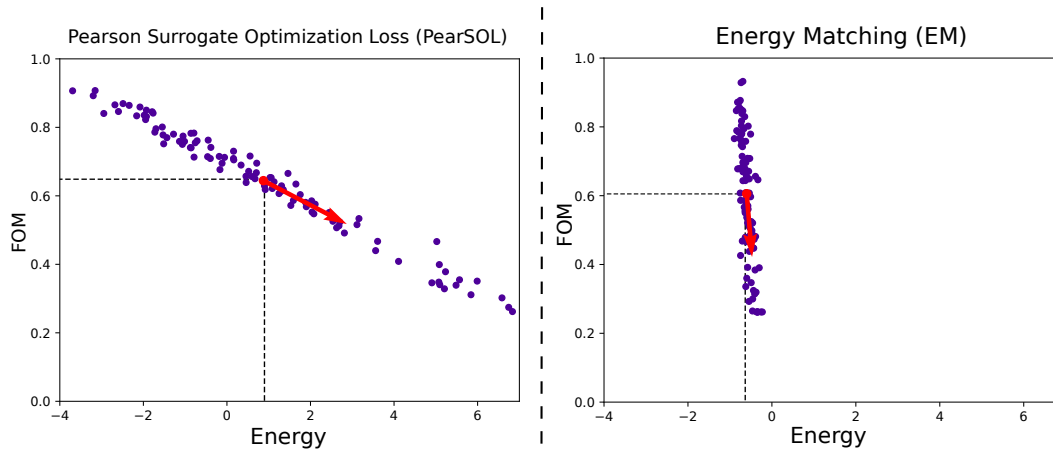


Figure 4: Comparing first principal component vectors and densities of Pearson Correlation and Energy Matching

erate improved designs while drastically reducing optimization time. The core contribution of PearSAN is the use of PearSOL as both a latent regularization method, similar to batch and layer normalization, and as a surrogate training loss. We compare both use cases with previous energy matching losses, which are shown to enforce poor regularization and performance, even with upgraded affine parameters. After 10 retraining iterations, we find that our PearSOL outperforms EM by VGG-predicted average FOM, (92.31% vs. 80.74%), and measures of generative quality, including KID, FID, and inception score. Additionally, we introduce an application of VCA and demonstrate its efficacy compared to SA in both convergence across annealing steps and ability to sample large datasets from the probabilities of the RNN. Our results demonstrate that PearSAN achieves a state-of-the-art maximum design efficiency of $\sim 97\%$, with a mean value of $\sim 71\%$. Compared to other methods, PearSAN is shown to be at least an order of magnitude faster, yielding both better generative performance metrics (e.g., KID, FID, Inception Score) and improved maximum figure of merit scores.

In short, PearSAN's blend of **surrogate modeling** and **annealing-based sampling** provides a powerful framework for high-dimensional, non-trivial design challenges. Its speed, flexibility, and high design quality make it a promising tool for accelerating innovation in renewable energy technologies, quantum information platforms, and beyond.

4.1 Future Directions

While we demonstrate PearSAN with a quadratic Boolean energy function, different physics-inspired energy models (e.g., Blume-Capel, Potts, or higher-order polynomials) may offer richer representations of the design space. Additionally, PearSAN can be adapted to continuous latent spaces (e.g., with a simple multilayer perceptron and the Adam optimizer [47].) Beyond autoregressive models for VCA, exploring different latent-space optimizers or advanced neural architectures such as State Space Machines [48] could further accelerate convergence. Beyond the TPV problem, the application of PearSAN to various nanophotonic device design tasks, such as quantum information and sensing, will help elucidate its generality and performance benefits.

Supporting Information

Supporting Information is available from the Wiley Online Library or from the author.

5 PearSOL vs EM

5.1 Pearson Correlation vs Energy Matching

Based on the set of latent vectors that represent the original thermal emitter designs, we use Principal Component Analysis (PCA) to compare Pearson Correlation and EM. Firstly, we determine the nature

of the correlation in both methods by analyzing the data's first principal components. The first principal component of the Pearson correlation is -0.063, and that of EM is -0.821. The negative values for both methods indicate an inverse (and thus, negative) correlation between the FOM and the energy. We then determine the correlation by finding the explained variance ratio between the first and second principal components of the data, i.e., $\frac{e_2}{e_1}$ where e_1 is the first component and e_2 is the second. A tighter correlation between components indicates that the first component captures a significantly larger proportion of the total variance, suggesting that the data is closely clustered around the first component. In the Pearson correlation, the first component explains 99.99% of the variance while the second component explains 0.0087% of the variance. Therefore, the first principal component explains an exceptionally high percentage of the variance compared to the second component. Conversely in EM, the first component explains 88.49% of the variance while the second component explains 11.51% of the variance. This evidently shows that the Pearson correlation establishes a stronger correlation between FOM and energy as opposed to EM.

5.2 PearSOL vs EM with Affine Parameters

We test whether adding positive variational affine parameters to the surrogate model, i.e., $\tilde{h}_\phi(\mathbf{z}) = \phi_\alpha h_\phi(\mathbf{z}) + \phi_\beta$, helps EM improve its latent optimization performance. The variance of reported FOM dramatically increases without a significant gain in FOM. Comparing affine EM with PearSOL in Figure 5, we see a similar trend. For both EM-affine experiments, one regularized with EM and one with PearSOL, EM either dramatically increases its variance (PearSOL regularized) or the FOM quality suffers (EM regularized). Due to the results in Figure 6, we conclude that it is better for EM to not use variational affine parameters. We expect the poor performance is likely due to increased difficulty of training ϕ_α . The gradient of the other parameters is also proportional to ϕ_α , resulting in greater variance in the gradient making convergence difficult. Even still, fine-tuning ϕ_α likely remains a challenging task.

6 Pearson Correlation Isotonicity

Consider a sample set $\{(x_1, y_1), \dots, (x_n, y_n)\}$ where $x_i, y_i \in \mathbb{R}$ given by evaluating the function $f : x \rightarrow y$. Strict isotonicity is given by $I(\hat{\mathbf{x}}) \prec_{\mathcal{X}}^+ f(\hat{\mathbf{x}})$:

$$\begin{aligned} x_i < x_j &\implies f(x_i) < f(x_j) \\ \iff x_i < x_j &\implies y_i < y_j, \end{aligned} \quad (18)$$

where I is the identity. Given two samples i, j , we can determine if strict isotonicity holds with an indicator,

$$\mathbf{m}(i, j) = (x_j < x_i \text{ and } y_j < y_i) \text{ or } (x_j > x_i \text{ and } y_j > y_i). \quad (19)$$

We know f is strictly isotonic if the differences along both axes, $(x_i - x_j) = \Delta x$ and $(y_i - y_j) = \Delta y$, have the same parity, i.e.,

$$\Delta x \Delta y > 0 \iff \mathbf{m}(i, j) = \mathbf{True}, \quad (20)$$

which can be seen in Fig. 7. This gives us a natural way to enforce isotonicity through the differentiable function

$$\gamma(X, Y) = \frac{1}{N^2} \sum_{i,j} \frac{(x_i - x_j)(y_i - y_j)}{\sigma_X \sigma_Y}. \quad (21)$$

If f is variational, then f can learn to be isotonic by maximizing $\gamma(X, Y)$. However, $\gamma(X, Y)$ is a point-wise function that scales $O(N^2)$. Instead, we use the Pearson correlation

$$\rho(X, Y) = \frac{1}{N} \sum_i \frac{(x_i - \bar{X})(y_i - \bar{Y})}{\sigma_X \sigma_Y}, \quad (22)$$

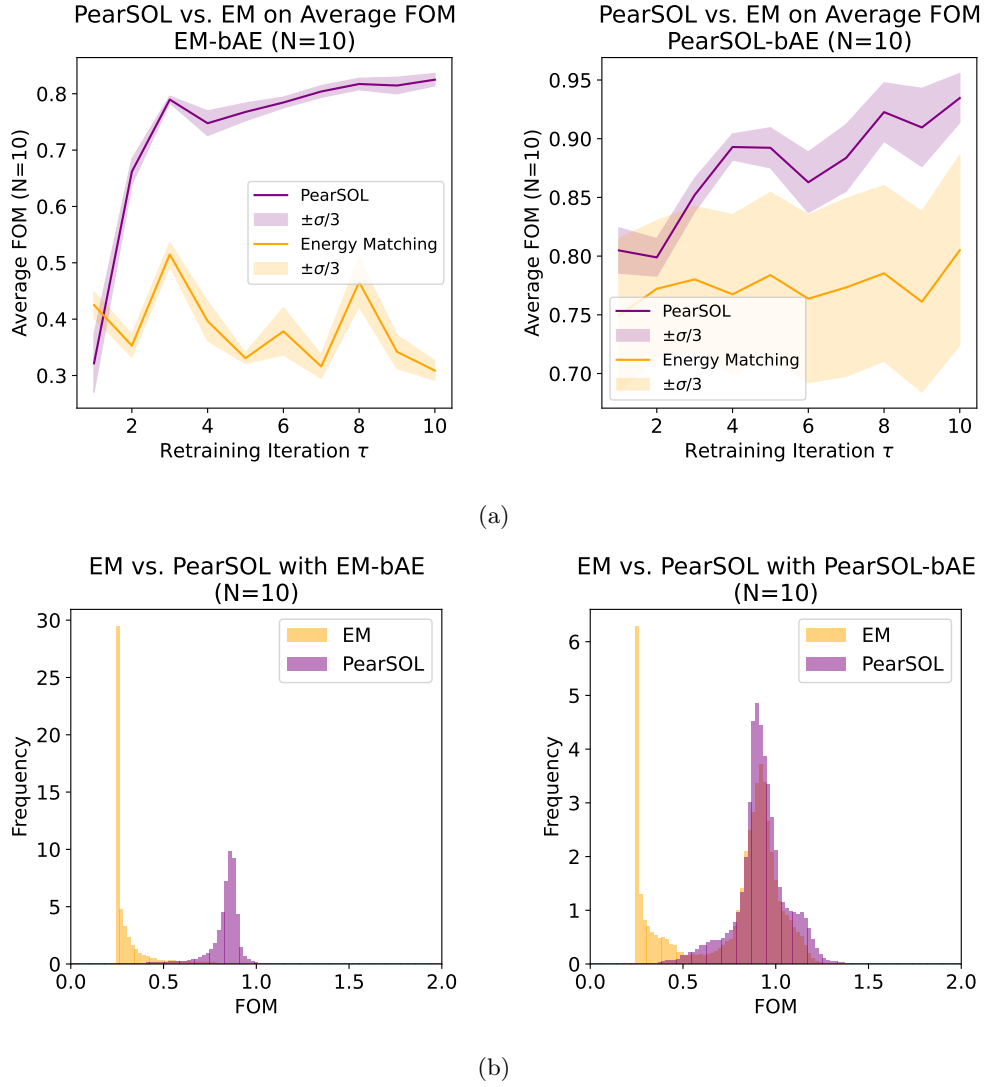


Figure 5: We compare PearSOL and EM (EM) regularization and surrogate model training with additional learnable affine parameters for EM. (a) Average VGGnet FOM Sampled from EM Regularized bAE and a PearSOL regularized bAE. (b) Histograms of the last training iteration from experiments in (a).

which can be shown to have bounded error with $\gamma_{X,Y}$ and only require $O(N)$ calculations. By expanding each summation, one can show that

$$\frac{1}{(n-1)}|\rho(X,Y) - \gamma(X,Y)| = \frac{|\text{Cov}(X,Y)|}{\sigma_X\sigma_Y} \leq 1 \quad (23)$$

where the inequality is given by Cauchy-Schwarz, i.e., $|\text{Cov}(X,Y)| \leq \sigma_X\sigma_Y$.

7 Pearson Correlational Loss

Within the PearSOL, the Pearson correlation $\mathcal{L}_{\text{Pearson}}$ is input into a supplemental inverse logistic curve:

$$\tilde{\mathcal{L}}_{\text{Pearson}} = \log\left(\frac{0.5(\mathcal{L}_{\text{Pearson}} + 1)}{1 - 0.5(\mathcal{L}_{\text{Pearson}} + 1)}\right). \quad (24)$$

This choice ensures that the gradient approaches infinity

$$\lim_{\rho_{xy} \rightarrow -1} \nabla \tilde{\mathcal{L}}_{\text{Pearson}} = \infty, \quad (25)$$

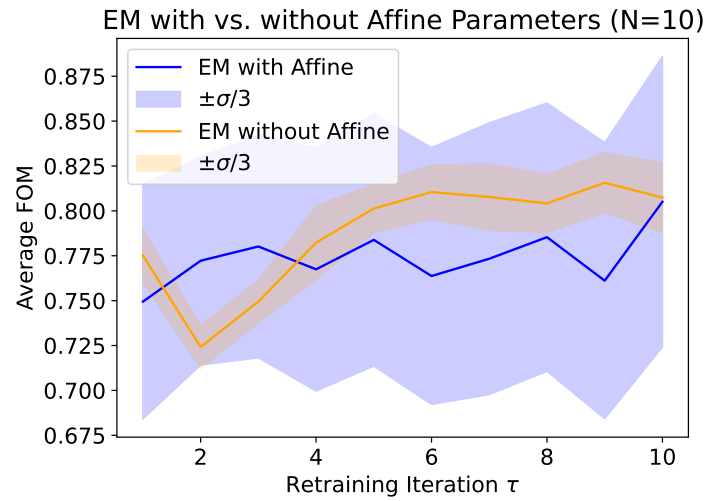


Figure 6: EM with and without affine parameters on the PearSOL regularized bAE.

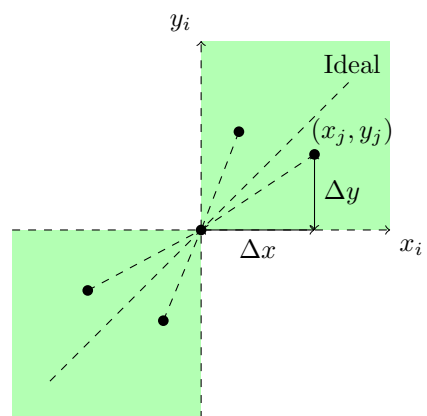


Figure 7: Isotonic, labeled Δx and Δy , with an ideal line passing through (x_i, y_i) .

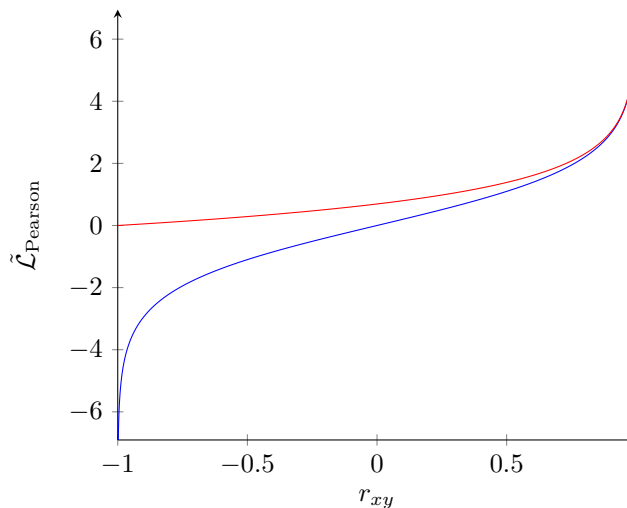


Figure 8: Graph of the supplemental inverse logistic curve utilized in correlational loss (blue) and the less rewarding logarithmic curve (red).

regardless of the weight λ chosen during training. In our experiments, we find that utilization of this curve consistently resulted in Pearson correlation coefficients closer to -1 as compared to no curve or the less rewarding logarithmic curve:

$$\tilde{\mathcal{L}}_{\text{Pearson}} = -\log(0.5(1 - \mathcal{L}_{\text{Pearson}})). \quad (26)$$

8 Binary Autoencoder Details

8.1 Binary Autoencoder

Because VCA samples a polynomial energy function over a binary space, we consider a binary autoencoder (bAE) to pre-train a decoder over a binary latent space. The bAE encoder $\mathcal{E}(\mathbf{x})$ generates a Bernoulli distribution $\mathcal{E}(\mathbf{x})_i = P(z_i = 1)$. After sampling $z_i = \text{Bernoulli}(\mathcal{E}(\mathbf{x})_i)$, a deterministic decoder $\mathcal{D}_\theta(\mathbf{z})$ constructs a new sample $\hat{\mathbf{x}}$. To train the bAE, we use the objective function

$$\mathcal{L}_{\text{bAE}} = \lambda_1 \|\mathbf{x} - \hat{\mathbf{x}}\|_2^2 + \lambda_2 \mathcal{L}_{\text{Perceptual}} + \lambda_3 \mathcal{L}_{\text{Reg}}, \quad (27)$$

which is a linear combination between standard mean-squared-error loss, the perceptual loss $\mathcal{L}_{\text{Perceptual}}$ [49]⁷, and either the EM or PearSOL losses \mathcal{L}_{Reg} which we now introduce. For more details on our implementation, see Appendix 8.

The dataset is symmetric under reflections about the the x and y axes. Hence, we only train on one quadrant of each design and use the reflection symmetry to regenerate the complete designs after sampling. We construct a binary autoencoder with residual blocks [50], attention layers [6], and sigmoid linear units [51]. The encoder utilizes 2D maxpooling operations to halve spatial dimensions and the decoder uses 2D transposed convolutions to double spatial dimensions. Residual blocks are implemented with two convolution operations and one skip connection from the input to the output. Following Vaswani et al. [6], we utilize scaled dot-product attention, implemented as:

$$\text{Attention}(Q, K, V) = \text{softmax}\left(\frac{QK^\top}{\sqrt{d_k}}\right)V. \quad (28)$$

Each model contains 4.2 million parameters, not including the surrogate energy function, and the models are trained for 10,000 epochs over the TPV dataset. We utilize Purdue University’s Gilbreth cluster, training each model with 12 NVIDIA A30 GPUs in parallel, with each model taking ≈ 15 hours. We find that we can achieve adequate reconstruction quality with a latent space of size 64, whereas [10] utilized a size of 256.

⁷Hyperparameter weights used in experiments listed in tabl 3.

Hyperparameter	Value
λ_1 (MSE)	0.6
λ_2 (Perceptual)	0.025
λ_3 (Correlation)	1e-3
λ_a (Pearson)	10.0
λ_b (Energy average)	0.01
λ_c (Norm)	10.0

Table 3: Hyperparameters used for joint training of bAE and energy function.

9 Annealing Implementations

Alternative to VCA, we implement simulated annealing as an alternative latent optimizer. Starting at initial temperature $T(0) = 1$, we linearly decreasing the temperature to $T(n) = 0$ over n iterations. We randomly initialize starting state s_0 , and for each annealing iteration, we randomly flip a single bit to produce candidate s' , and we calculate the acceptance probability according to the Metropolis-Hastings rule:

$$A(s'|s_t) = \min\left(1, \exp\left\{\frac{E(s_t) - E(s')}{T(t)}\right\}\right). \quad (29)$$

In our comparison to VCA, we set $n = 200$ for both methods and maintain the same linear temperature schedule. For our VCA implementation, we calculate the variational free energy loss by drawing $N_s = 50$ discrete samples from the model probabilities. We transition to the next state after each gradient descent step.

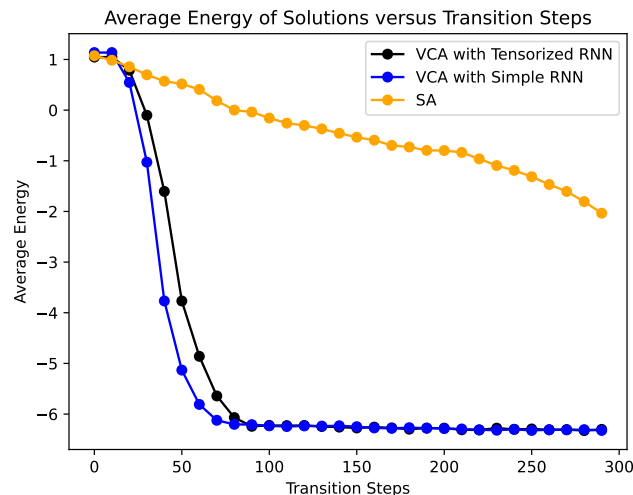


Figure 9: Comparison of VCA with tensorized layers, VCA with concatenation layers, and SA across second order polynomial surrogate model trained through correlational loss. Whereas Hibat-Allah et al. [29] find in their applications that the tensorized RNN exhibits better convergence, we observe similar behavior between tensorized and concatenation operations. Both forms of VCA converge significantly faster than SA. The VCA models are implemented with 1D RNNs, and VCA and SA models use the same linear temperature schedule, decreasing from 1 to 0 over the training iterations.

We additionally compare concatenation-based VCA, tensorized VCA, and SA in Figure 9, finding that both forms of VCA demonstrate far superior convergence to SA; however, with our surrogate model, the concatenation-based and tensorized VCA models performed similarly, contrasting the findings by Hibat et al., demonstrating superior results of tensorized RNN cells on a uniform ferromagnetic Ising chain model.

10 Retraining Procedure Further Details

In our retraining procedure, we alternate between training the surrogate model to predict FOM from vectors and using VCA to discover new latent vectors, where we calculate their decoded efficiencies and append the vector-efficiency pair to the existing dataset.

Hyperparameter	Value
τ_{\max}	10
N_{thresh}	20
Surrogate Model Retraining Epochs	300
VCA Iterations	100
Surrogate Model Learning Rate	1e-5
VCA Learning Rate	5e-4
EM affine parameter lr	1e-3
EM and PearSOL lr	1e-5

Table 4: Hyperparameter values used in the retraining procedure.

Acknowledgements

This work is supported by the U.S. Department of Energy (DOE), Office of Science through the Quantum Science Center (QSC), a National Quantum Information Science Research Center (algorithm development) and Purdue’s Elmore ECE Emerging Frontiers Center “The Crossroads of Quantum and AI.”

References

- [1] I. J. Goodfellow, J. Pouget-Abadie, M. Mirza, B. Xu, D. Warde-Farley, S. Ozair, A. Courville, Y. Bengio, Generative Adversarial Networks, **2014**, URL <http://arxiv.org/abs/1406.2661>.
- [2] J. Jiang, D. Sell, S. Hoyer, J. Hickey, J. Yang, J. A. Fan, *ACS Nano* **2019**, *13*, 8 8872.
- [3] C. Pabbaraju, D. Rohatgi, A. Sevekari, H. Lee, A. Moitra, A. Risteski, Provable benefits of score matching, **2023**, URL <https://arxiv.org/abs/2306.01993>.
- [4] A. Ramesh, M. Pavlov, G. Goh, S. Gray, C. Voss, A. Radford, M. Chen, I. Sutskever, Zero-Shot Text-to-Image Generation, **2021**, URL <https://arxiv.org/abs/2102.12092>.
- [5] R. Rombach, A. Blattmann, D. Lorenz, P. Esser, B. Ommer, High-Resolution Image Synthesis with Latent Diffusion Models, **2022**, URL <http://arxiv.org/abs/2112.10752>.
- [6] A. Vaswani, N. Shazeer, N. Parmar, J. Uszkoreit, L. Jones, A. N. Gomez, L. Kaiser, I. Polosukhin, Attention Is All You Need, **2017**, URL <http://arxiv.org/abs/1706.03762>.
- [7] OpenAI, J. Achiam, S. Adler, S. Agarwal, L. Ahmad, I. Akkaya, F. L. Aleman, D. Almeida, J. Al-tenschmidt, S. Altman, S. Anadkat, R. Avila, I. Babuschkin, S. Balaji, V. Balcom, P. Baltescu, H. Bao, M. Bavarian, J. Belgum, I. Bello, J. Berdine, G. Bernadett-Shapiro, C. Berner, L. Bogdonoff, O. Boiko, M. Boyd, A.-L. Brakman, G. Brockman, T. Brooks, M. Brundage, K. Button, T. Cai, R. Campbell, A. Cann, B. Carey, C. Carlson, R. Carmichael, B. Chan, C. Chang, F. Chantzis, D. Chen, S. Chen, R. Chen, J. Chen, M. Chen, B. Chess, C. Cho, C. Chu, H. W. Chung, D. Cummings, J. Currier, Y. Dai, C. Decareaux, T. Degry, N. Deutsch, D. Deville, A. Dhar, D. Dohan, S. Dowling, S. Dunning, A. Ecoffet, A. Eleti, T. Eloundou, D. Farhi, L. Fedus, N. Felix, S. P. Fishman, J. Forte, I. Fulford, L. Gao, E. Georges, C. Gibson, V. Goel, T. Gogineni, G. Goh, R. Gontijo-Lopes, J. Gordon, M. Grafstein, S. Gray, R. Greene, J. Gross, S. S. Gu, Y. Guo, C. Hallacy, J. Han, J. Harris, Y. He, M. Heaton, J. Heidecke, C. Hesse, A. Hickey, W. Hickey, P. Hoeschele, B. Houghton, K. Hsu, S. Hu, X. Hu, J. Huizinga, S. Jain, S. Jain, J. Jang, A. Jiang, R. Jiang, H. Jin, D. Jin, S. Jomoto, B. Jonn, H. Jun, T. Kaftan, L. Kaiser,

- A. Kamali, I. Kanitscheider, N. S. Keskar, T. Khan, L. Kilpatrick, J. W. Kim, C. Kim, Y. Kim, J. H. Kirchner, J. Kiros, M. Knight, D. Kokotajlo, L. Kondraciuk, A. Kondrich, A. Konstantinidis, K. Kosic, G. Krueger, V. Kuo, M. Lampe, I. Lan, T. Lee, J. Leike, J. Leung, D. Levy, C. M. Li, R. Lim, M. Lin, S. Lin, M. Litwin, T. Lopez, R. Lowe, P. Lue, A. Makanju, K. Malfacini, S. Manning, T. Markov, Y. Markovski, B. Martin, K. Mayer, A. Mayne, B. McGrew, S. M. McKinney, C. McLeavey, P. McMillan, J. McNeil, D. Medina, A. Mehta, J. Menick, L. Metz, A. Mishchenko, P. Mishkin, V. Monaco, E. Morikawa, D. Mossing, T. Mu, M. Murati, O. Murk, D. Mély, A. Nair, R. Nakano, R. Nayak, A. Neelakantan, R. Ngo, H. Noh, L. Ouyang, C. O’Keefe, J. Pachocki, A. Paino, J. Palermo, A. Pantuliano, G. Parascandolo, J. Parish, E. Parparita, A. Passos, M. Pavlov, A. Peng, A. Perelman, F. d. A. B. Peres, M. Petrov, H. P. d. O. Pinto, Michael, Pokorny, M. Pokrass, V. H. Pong, T. Powell, A. Power, B. Power, E. Proehl, R. Puri, A. Radford, J. Rae, A. Ramesh, C. Raymond, F. Real, K. Rimbach, C. Ross, B. Rotsted, H. Roussez, N. Ryder, M. Saltarelli, T. Sanders, S. Santurkar, G. Sastry, H. Schmidt, D. Schnurr, J. Schulman, D. Sel-sam, K. Sheppard, T. Sherbakov, J. Shieh, S. Shoker, P. Shyam, S. Sidor, E. Sigler, M. Simens, J. Sitkin, K. Slama, I. Sohl, B. Sokolowsky, Y. Song, N. Staudacher, F. P. Such, N. Summers, I. Sutskever, J. Tang, N. Tezak, M. B. Thompson, P. Tillet, A. Tootoonchian, E. Tseng, P. Tug-gle, N. Turley, J. Tworek, J. F. C. Uribe, A. Vallone, A. Vijayvergiya, C. Voss, C. Wainwright, J. J. Wang, A. Wang, B. Wang, J. Ward, J. Wei, C. Weinmann, A. Welihinda, P. Welinder, J. Weng, L. Weng, M. Wiethoff, D. Willner, C. Winter, S. Wolrich, H. Wong, L. Workman, S. Wu, J. Wu, M. Wu, K. Xiao, T. Xu, S. Yoo, K. Yu, Q. Yuan, W. Zaremba, R. Zellers, C. Zhang, M. Zhang, S. Zhao, T. Zheng, J. Zhuang, W. Zhuk, B. Zoph, GPT-4 Technical Report, **2023**, URL <https://arxiv.org/abs/2303.08774>.
- [8] S. Minaee, T. Mikolov, N. Nikzad, M. Chenaghlu, R. Socher, X. Amatriain, J. Gao, Large Language Models: A Survey, **2024**, URL <http://arxiv.org/abs/2402.06196>.
- [9] S. Dara, S. Dhamercherla, S. S. Jadav, C. M. Babu, M. J. Ahsan, *Artificial Intelligence Review* **2022**, *55*, 3 1947.
- [10] B. A. Wilson, Z. A. Kudyshev, A. V. Kildishev, S. Kais, V. M. Shalaev, A. Boltasseva, *Applied Physics Reviews* **2021**, *8*, 4 041418.
- [11] B. A. Wilson, J. Wurtz, V. Mkhitarian, M. Bezick, S.-T. Wang, S. Kais, V. M. Shalaev, A. Boltasseva, Non-native Quantum Generative Optimization with Adversarial Autoencoders, **2024**, URL <https://arxiv.org/abs/2407.13830>.
- [12] D. Brunner, M. C. Soriano, S. Fan, *Nanophotonics* **2023**, *12*, 5 773.
- [13] B. Wilson, Y. Chen, D. Kumar Singh, R. Ojha, J. Pottle, M. Bezick, A. Boltasseva, V. M. Shalaev, A. V. Kildishev, *Advanced Photonics* **2024**, *6*, 05.
- [14] J. Jiang, J. A. Fan, *Nano Letters* **2019**, *19*, 8 5366.
- [15] Z. A. Kudyshev, A. V. Kildishev, V. M. Shalaev, A. Boltasseva, *Applied Physics Reviews* **2020**, *7*, 2 021407.
- [16] L. Mascaretti, Y. Chen, O. Henrotte, O. Yesilyurt, V. M. Shalaev, A. Naldoni, A. Boltasseva, *ACS Photonics* **2023**, *10*, 12 4079.
- [17] Z. A. Kudyshev, A. V. Kildishev, V. M. Shalaev, A. Boltasseva, *Nanophotonics* **2021**, *10*, 1 371.
- [18] B. Wilson, Y. Chen, S. Kais, A. Kildishev, V. Shalaev, A. Boltasseva, In *Quantum 2.0 Conference and Exhibition*. Optica Publishing Group, Boston, MA, ISBN 978-1-957171-11-1, **2022** QTu2A.13, URL <https://opg.optica.org/abstract.cfm?URI=QUANTUM-2022-QTu2A.13>.
- [19] W. Ma, F. Cheng, Y. Xu, Q. Wen, Y. Liu, *Advanced Materials* **2019**, *31*, 35 1901111.

- [20] S. Tabassum, S. Nayemuzzaman, M. Kala, A. Kumar Mishra, S. K. Mishra, *Sensors* **2022**, *22*, 18 6896.
- [21] P. Georgi, M. Massaro, K.-H. Luo, B. Sain, N. Montaut, H. Herrmann, T. Weiss, G. Li, C. Silberhorn, T. Zentgraf, *Light: Science & Applications* **2019**, *8*, 1 70.
- [22] J. Qin, S. Jiang, Z. Wang, X. Cheng, B. Li, Y. Shi, D. P. Tsai, A. Q. Liu, W. Huang, W. Zhu, *ACS Nano* **2022**, *16*, 8 11598.
- [23] A. J. Ollanik, R. Bushati, D. Gaudiosi, J. Zultak, M. Krogstad, M. Bohn, W. Zhu, A. Agrawal, H. Lezec, M. Rowe, In *CLEO 2024 (2024)*, paper ATh5A.7. Optica Publishing Group, **2024** ATh5A.7, URL https://opg.optica.org/abstract.cfm?uri=CLEO_AT-2024-ATh5A.7.
- [24] A. N. M. T. Elahi, K. Park, In M. P. Mengüç, M. Francoeur, editors, *Light, Plasmonics and Particles*, Nanophotonics, 443–470. Elsevier, ISBN 978-0-323-99901-4, **2023**, URL <https://www.sciencedirect.com/science/article/pii/B978032399901400024X>.
- [25] R. E. Christiansen, O. Sigmund, *Journal of the Optical Society of America B* **2021**, *38*, 2 496.
- [26] S. Kirkpatrick, C. D. Gelatt, M. P. Vecchi, *Science* **1983**, *220*, 4598 671.
- [27] A. Rajak, S. Suzuki, A. Dutta, B. K. Chakrabarti, *Philosophical Transactions of the Royal Society A: Mathematical, Physical and Engineering Sciences* **2023**, *381*, 2241 20210417.
- [28] E. Jang, S. Gu, B. Poole, Categorical Reparameterization with Gumbel-Softmax, **2017**, URL <http://arxiv.org/abs/1611.01144>.
- [29] M. Hibat-Allah, E. M. Inack, R. Wiersema, R. G. Melko, J. Carrasquilla, *Nature Machine Intelligence* **2021**, *3*, 11 952.
- [30] D. Bank, N. Koenigstein, R. Giryes, Autoencoders, **2021**, URL <http://arxiv.org/abs/2003.05991>.
- [31] D. P. Kingma, M. Welling, Auto-Encoding Variational Bayes, **2022**, URL <http://arxiv.org/abs/1312.6114>.
- [32] A. Khoshaman, W. Vinci, B. Denis, E. Andriyash, H. Sadeghi, M. H. Amin, *Quantum Science and Technology* **2018**, *4*, 1 014001.
- [33] Z. Wang, J. Wang, Z. Liu, Q. Qiu, Binary Latent Diffusion, **2023**, URL <http://arxiv.org/abs/2304.04820>.
- [34] S. Boixo, T. F. Rønnow, S. V. Isakov, Z. Wang, D. Wecker, D. A. Lidar, J. M. Martinis, M. Troyer, *Nature Physics* **2014**, *10*, 3 218.
- [35] A. Lucas, *Frontiers in Physics* **2014**, *2*.
- [36] W. De Mulder, S. Bethard, M.-F. Moens, *Computer Speech & Language* **2015**, *30*, 1 61.
- [37] L. Basora, X. Olive, T. Dubot, *Aerospace* **2019**, *6*, 11 117.
- [38] J. M. Ackerson, D. Rushit, S. Jim, Applications of Recurrent Neural Network for Biometric Authentication & Anomaly Detection, **2021**, URL <http://arxiv.org/abs/2109.05701>.
- [39] J. Benesty, J. Chen, Y. Huang, I. Cohen, In *Noise Reduction in Speech Processing*, volume 2, 1–4. Springer Berlin Heidelberg, Berlin, Heidelberg, ISBN 978-3-642-00295-3 978-3-642-00296-0, **2009**, URL http://link.springer.com/10.1007/978-3-642-00296-0_5.
- [40] J. Lu, Y. Tian, S. Wang, M. Sheng, X. Zheng, PearNet: A Pearson Correlation-based Graph Attention Network for Sleep Stage Recognition, **2022**, URL <http://arxiv.org/abs/2209.13645>, ArXiv:2209.13645 [cs, eess].

- [41] A. A. Khairul Azri, M. S. Mohd Jasni, S. F. Wan Muhamad Hatta, M. A. Islam, Y. Abdul Wahab, S. Mekhilef, P. J. Ker, *Solar Energy* **2023**, 259–279.
- [42] R. Sakakibara, V. Stelmakh, W. R. Chan, M. Ghebrehbrhan, J. D. Joannopoulos, M. Soljacic, I. Čelanović, *Journal of Photonics for Energy* **2019**, 9, 3 032713.
- [43] M. Bińkowski, D. J. Sutherland, M. Arbel, A. Gretton, Demystifying MMD GANs, **2021**, URL <http://arxiv.org/abs/1801.01401>.
- [44] M. Heusel, H. Ramsauer, T. Unterthiner, B. Nessler, S. Hochreiter, GANs Trained by a Two Time-Scale Update Rule Converge to a Local Nash Equilibrium, **2018**, URL <http://arxiv.org/abs/1706.08500>.
- [45] T. Salimans, I. Goodfellow, W. Zaremba, V. Cheung, A. Radford, X. Chen, Improved Techniques for Training GANs, **2016**, URL <http://arxiv.org/abs/1606.03498>.
- [46] S. Frolov, T. Hinz, F. Raue, J. Hees, A. Dengel, *Neural Networks* **2021**, 144–187.
- [47] D. P. Kingma, J. Ba, Adam: A method for stochastic optimization, **2017**, URL <https://arxiv.org/abs/1412.6980>.
- [48] A. Gu, T. Dao, Mamba: Linear-time sequence modeling with selective state spaces, **2024**, URL <https://arxiv.org/abs/2312.00752>.
- [49] R. Zhang, P. Isola, A. A. Efros, E. Shechtman, O. Wang, The Unreasonable Effectiveness of Deep Features as a Perceptual Metric, **2018**, URL <http://arxiv.org/abs/1801.03924>.
- [50] K. He, X. Zhang, S. Ren, J. Sun, Deep Residual Learning for Image Recognition, **2015**, URL <http://arxiv.org/abs/1512.03385>.
- [51] S. Elfving, E. Uchibe, K. Doya, Sigmoid-Weighted Linear Units for Neural Network Function Approximation in Reinforcement Learning, **2017**, URL <http://arxiv.org/abs/1702.03118>.